ACS NANO

www.acsnano.org

ARTICLE

High-Quality Hexagonal Boron Nitride from 2D Distillation

Huanyao Cun,*,§ Zichun Miao,§ Adrian Hemmi, Yasmine Al-Hamdani, Marcella Iannuzzi, Jürg Osterwalder, Michael S. Altman, and Thomas Greber

Cite This: *ACS Nano* 2021, 15, 1351−1357

Read Online

ACCESS | Metrics & More | Article Recommendations | Supporting Information

ABSTRACT: **The production of high-quality two-dimensional (2D) materials is essential for the ultimate performance of single layers and their hybrids. Hexagonal boron nitride (*h*-BN) is foreseen to become the key 2D hybrid and packaging material since it is insulating, impermeable, flat, transparent, and chemically inert, though it is difficult to attain in ultimate quality. Here, a scheme is reported for producing single layer *h*-BN that shows higher quality in view of mosaicity and strain variations than material from chemical vapor deposition (CVD). We delaminate CVD *h*-BN from Rh(111) and transfer it to a clean metal surface. The twisting angle between BN and the second substrate yields metastable moiré structures. Annealing above 1000 K leads to 2D distillation, *i.e.*, catalyst-assisted BN sublimation from the edges of the transferred layer and subsequent condensation into superior quality *h*-BN. This provides a way for 2D material production remote from CVD instrumentation.**

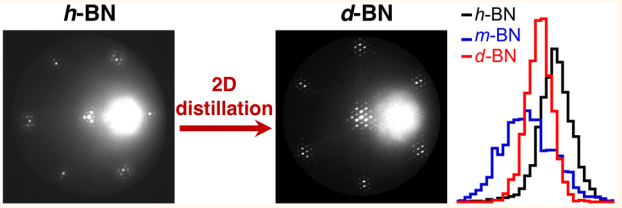

KEYWORDS: *h-BN, 2D materials transfer, moiré, heterogeneous catalysis, 2D distillation*

INTRODUCTION

The paradigm "two-dimensional (2D) materials"[1] is expected to enable opportunities for devices with ultimately thin membranes,[2] mechanical detectors,[3] inks,[4] and specifically for electronics beyond silicon technology.[5,6] These materials can be assembled at room temperature, layer by layer, which allows us to produce nonequilibrium hybrid structures. For instance, the twisting of two stacked graphene layers leads to 2D superconductivity that is related to the moiré interference between the two 2D lattices.[7]

Before harvesting the benefits of materials, their fabrication and handling have to be mastered. This is a big challenge for 2D materials since they mostly consist of surfaces that are known to be prone to imperfections like contaminations and defects. The related reactivity of 2D materials calls for a packaging material that is protective, impermeable, thin, flat, transparent, and nonreactive. Hexagonal boron nitride (*h*-BN) has all these properties and is the prime candidate to become the key 2D packaging and hybrid material.[8] Currently, the main approach for scalable production is chemical vapor deposition (CVD) of precursors that contain boron and nitrogen[9−14] and segregation-assisted growth[15,16] on substrates acting as catalysts or bulk reservoirs of B and N.[17] Although CVD does not allow the preparation of single orientation *h*-BN on all substrates, transfer of single-orientation *h*-BN does, with the added feature of nonequilibrium moiré formation with arbitrary lattice orientation. However, transfer is another challenge, since it is, if successful, often accompanied by compromises to the material quality.[18,19]

In view of these problems and opportunities, we transferred CVD-grown single layer boron nitride back onto a crystalline catalyst. The introduction of a twist angle enables moiré interference between the second substrate and the *h*-BN layer. Annealing of such structures reveals the temperature window, within which this moiré structure is efficiently cleaned and stable. At higher temperatures this metastable moiré undergoes a phase transformation where boron nitride sublimates from the edge of the transferred BN into a dilute adsorbate phase and a recondensation into a lattice aligned higher quality *h*-BN. Because the sublimation and recondensation processes are well confined to the substrate surface, we label it "2D distillation". This is a way to produce *h*-BN from transferred material with holes and contaminations and remote from CVD equipment. All these products and processes can be directly monitored in real time with low energy electron microscopy (LEEM).

Single orientation *h*-BN monolayers on rhodium, also called "nanomesh",[10,20] are fabricated in a CVD process on single

Received: October 15, 2020
Accepted: December 16, 2020
Published: December 30, 2020

https://dx.doi.org/10.1021/acsnano.0c08616
ACS Nano 2021, 15, 1351−1357

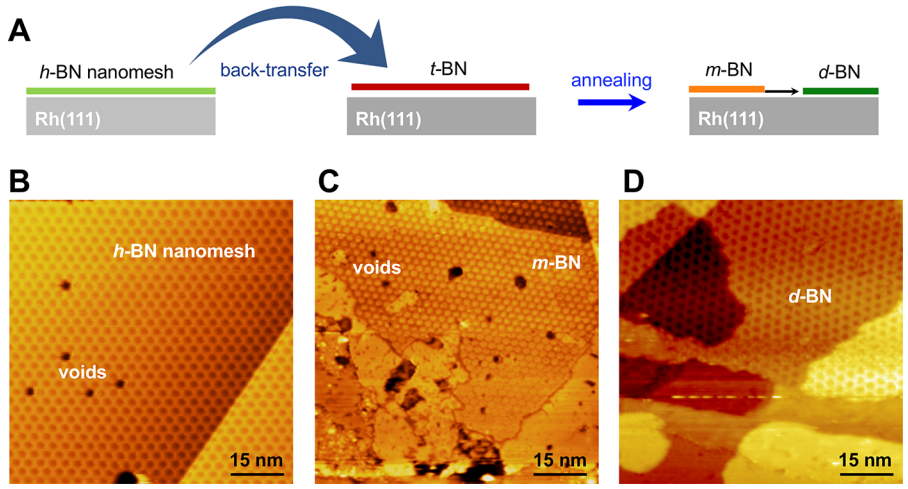

Figure 1. Transfer and annealing of *h*-BN on Rh(111). (A) Concept: After growth and delamination, the *h*-BN monolayer is transferred on a Rh(111) substrate, where *t*-BN forms. Annealing of *t*-BN leads to visible moiré structures (*m*-BN), and at higher temperature *m*-BN distills into *d*-BN; *i.e.*, nanomesh reforms; (B-D) Room temperature STM (80 × 80 nm^2) images of pristine *h*-BN nanomesh with 2 nm voids on Rh(111) (B), *m*-BN with voids on Rh(111) after transfer and annealing to 750 K (C), and distilled *m*-BN without voids on Rh(111) (*d*-BN) after transferred and annealing above 1000 K (D). $U = -1.20$ V, $I = 0.50$ nA.

crystalline Rh(111) at a 4-in. wafer scale.[21] As on Ru(0001),[22] the interaction of BN with the substrate is relatively strong and aligned *h*-BN can be grown while, *e.g.*, no pronounced azimuthal lock-in was observed for Pd(111).[23]

RESULTS AND DISCUSSION

Figure 1A depicts the procedure of the experiments. After CVD growth, a *h*-BN monolayer was transferred (named *t*-BN) on arbitrary substrates.[18,19] Here, we investigate the transfer of *h*-BN onto Rh(111). X-ray photoelectron spectroscopy (XPS) data in Figure S1 of the Supporting Information (SI) confirms successful transfer of *h*-BN layer. Notably the lattices of *t*-BN and the Rh substrate are not aligned, as is the case for the *h*-BN nanomesh. Annealing to 750 K cleans the surface, which induces the formation of moiré structures (*m*-BN) that can be resolved with scanning tunneling microscopy (STM). The *m*-BN is metastable, and annealing to higher temperatures leads to a more stable phase (*d*-BN): the process that we call "2D distillation". The process is robust and was observed for all *m*-BN moiré structures with twist angles between 4 and 25° that were investigated. Figure 1B shows a STM image of a CVD-grown *h*-BN nanomesh on Rh(111).[10] Prior to the imaging, 2 nm voids have been created with the "can-opener" effect[24,25] in order to have the fingerprint of the original BN layer after transfer.[18] Figure 1C displays a representative STM image of *m*-BN with such 2 nm voids. Clearly, a hexagonal superlattice is distinguished. Compared to the nanomesh in Figure 1B, the moiré lattice constant is 25% smaller, and the unit cell displays a 0.1 nm protrusion and not a depression (more data can be found in Figure S2 of the SI). Applying the theory for a periodic overlayer moiré pattern,[26] the superlattice constant of 2.4 nm indicates that this transferred *t*-BN flake was rotated by $\alpha = 4°$ with respect to the Rh lattice. Figure 1D shows a region of the surface after further annealing to above 1000 K. The formation of a superstructure with a lattice constant of 3.2 nm, which is within the error bar of the *h*-BN nanomesh, is observed. Furthermore, the 2 nm voids as seen in Figure 1B,C disappeared.

For the study of macro- and mesoscopic properties of transferred BN at the millimeter scale, other methods than STM have to be employed. While low energy electron diffraction (LEED) maps the macroscopic crystallinity, ultraviolet photoelectron spectroscopy (UPS) provides details on the electronic structures. An *m*-BN sample with a lattice rotation angle $\alpha = 19°$ and a transfer rate of 95% is compared with a nanomesh ($\alpha = 0°$) in Figure 2. The moiré is formed after transfer and annealing to 750 K. The angle α between the $[1\bar{1}0]$ direction of the substrate and the [10] direction of the adsorbate is determined from the LEED patterns in Figure 2A,B. Normal emission angle-resolved photoemission spectroscopy (ARPES) displays a σ band splitting $\Delta_{\alpha'\beta'}$ of 0.6 eV for this *m*-BN and an upshift $\Delta_{\alpha\alpha'}$ of the σ_α bands by 0.27 eV to 4.27 eV binding energy. This upshift is in line with the *h*-BN physisorption picture,[9] which indicates for the present case that the work function of the $\alpha = 19°$ moiré is 0.2 eV higher than that of the *h*-BN nanomesh. The σ_α and σ_β band-positions are measures for the electrostatic potential variations in the boron nitride supercell, and it can be seen that this splitting decreases by about a factor of 2 from the nanomesh to the $\alpha = 19°$ moiré. The fact that the supercell lattice constant decreases by a factor of 4.24 implies even larger lateral electric fields than in the *h*-BN nanomesh.[27] The interpretation of the photoemission results is supported by density functional theory (DFT) with the calculation of 19 *h*-BN units rotated by an angle of 23.4° on top of a (4 × 4) Rh unit cell. It predicts that the bonding of the rotated *h*-BN layer with the substrate is about 20% weaker than the aligned 169 on 144 R0° *h*-BN/Rh(111) nanomesh (see S4.1 in the SI).[28]

The properties of 2D materials strongly depend on their lattice: strain fluctuations and lattice rotation angle distributions at the micrometer scale are decisive. For the case of graphene lattice, strain may be measured with Raman spectroscopy.[29,30] If it comes to a noninvasive method that captures the lattice rotation and the related moiré angles on the mesoscopic scale, LEEM gives direct insight.[31−36] LEEM identifies different phases in bright field images, where the specular electron reflectivity is measured, while the local crystal lattice orientation and straining can be inferred from μ-LEED

https://dx.doi.org/10.1021/acsnano.0c08616
ACS Nano 2021, 15, 1351−1357

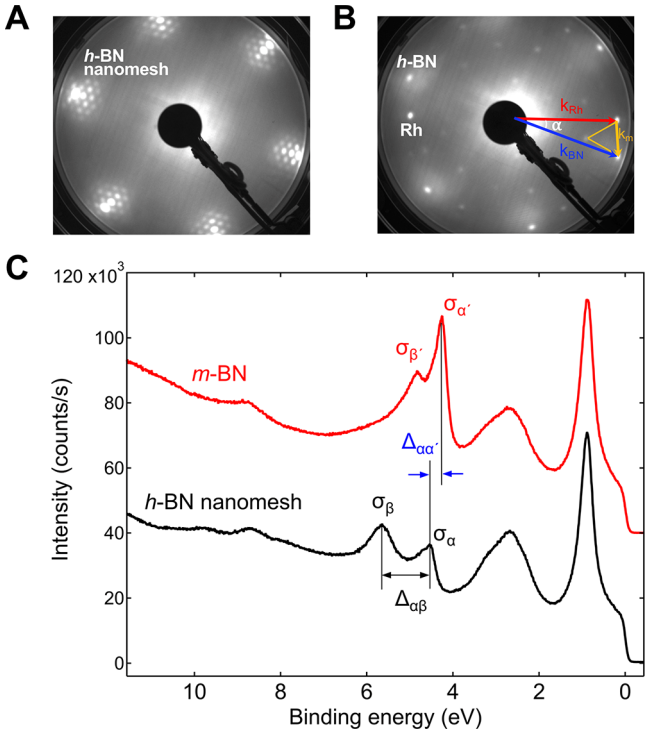

Figure 2. Structural and electronic properties of *h*-BN/Rh(111) and *m*-BN/Rh(111). (A, B) LEED patterns (E = 70 eV) of pristine *h*-BN nanomesh (A), and transferred *h*-BN on Rh(111) after annealing to 750 K (*m*-BN) (B). The reciprocal lattice vectors of Rh(111), *h*-BN, and the superstructures are indicated. The angle α between the substrate $\vec{k}_{Rh}$ (red) and *h*-BN ⟨10⟩ diffraction spots $\vec{k}_{BN}$ (blue) is 19°. $\vec{k}_{BN}-\vec{k}_{Rh}$ is the reciprocal moiré lattice vector $\vec{k}_m$ (orange). (C) UPS (He I_α) spectra of pristine *h*-BN nanomesh (black) and *m*-BN (red) in (B). The work function increase of *m*-BN/Rh(111) is reflected in the σ band shift $\Delta_{\alpha\alpha'}$. The σ-band splitting $\Delta_{\alpha\beta}$ is smaller in *m*-BN.

diffraction patterns measured on 250 nm length scale.[36] Furthermore, LEEM can be performed at high temperatures, which allows us to directly observe phase transformations from *t*-BN into *d*-BN in real space and time.

Figure 3 shows LEEM data from a single layer *h*-BN with 2 nm voids that was transferred on a Rh(111) thin film substrate and annealed to different temperatures. Figure 3A discerns *t*-BN and *m*-BN phases within the field-of-view of 23 μm at 1130 K. The transformation reaction starts at catalytic particle sites (condensation seed, see S5.2 and Figure S7 in the SI). The zoom-in area (yellow dashed circle in Figure 3A,F) in Figure 3B–E document the 2D distillation process of *m*-BN to *d*-BN and show that the reaction proceeds with speeds in the order of 10 nm/s without the presence of BN precursor molecules in the gas phase and with less than 50% loss of BN (see the LEEM movie and analysis details in S5.1 of the SI). Since boron binds more strongly to Rh(111) than nitrogen does (see section 4.2 of the SI), a supply of nitrogen from the gas phase could decrease the loss of BN due to N desorption during distillation. This is also a hint that the observed $(2\sqrt{3} \times 2\sqrt{3})$R30° superstructure on the bare rhodium near *d*-BN (see Figure S8 in the SI) is a boron-induced reconstruction. The distillation occurred on a tens of micron length scale at numerous independent locations on the sample, limited by the annealing time. In Figure 3F, the *d*-BN structure dominates, where straight segments at the edges of the *d*-BN patches

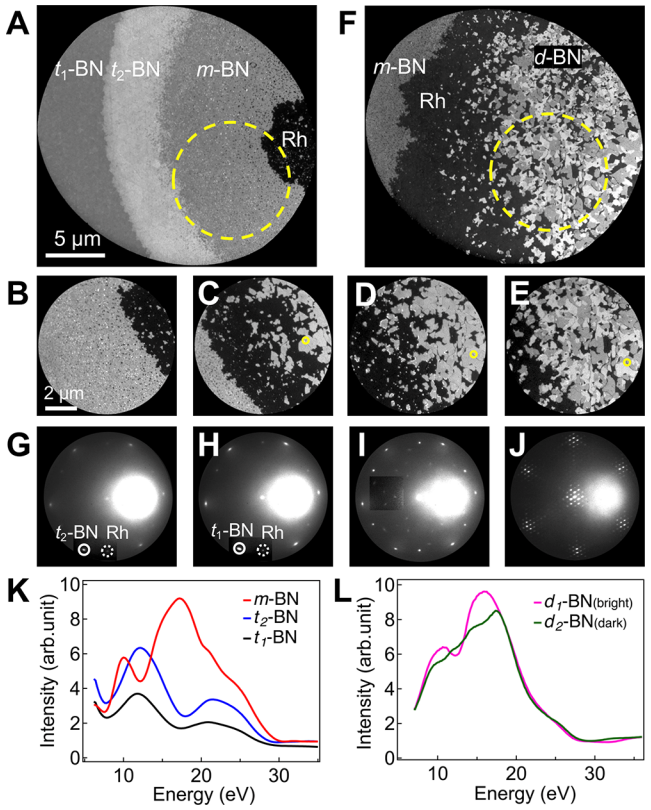

Figure 3. Low electron energy microscopy (LEEM) images, patterns and spectra. (A–F) LEEM bright-field image sequence of the transformation from *t*-BN to *m*-BN, and 2D distillation to *d*-BN upon annealing (see LEEM video in the SI). The yellow circle in C–E is a marker at the same location on the sample to guide the viewers for how the *d*-BN evolves: (A) 1130 K, t = 0; (B) 1135 K, t = 11 min; (C) 1180 K, t = 19 min; (D) 1180 K, t = 28 min; (E) 1210 K, t = 38 min; (F) 1210 K, t = 47 min. (B–E) Zoom-ins of the area indicated by the yellow dashed-circles in (A) and (F). The imaging energies are 12 eV in (A)–(D) and 15 eV in (E) and (F). The μ-LEED patterns of (G) t_2-BN, (H) t_1-BN, (I) *m*-BN, and (J) *d*-BN were recorded at room temperature after annealing to 1100 K (G–I) and 1210 K (J). t_2-BN, t_1-BN, and Rh spots are highlighted by white solid-line and dashed-line circles in (G) and (H). (K, L) LEEM I(V) spectra of different phases are measured after recording the corresponding μ-LEED patterns. (K) t_1-BN (black), t_2-BN (blue), and *m*-BN (red). (L) *d*-BN twin domains of d_1 (magenta) and d_2 (green).

reveal the crystallographic orientation of the *d*-BN. Furthermore, *d*-BN exhibits two intensities in Figure 3F that identify BN/substrate twinning domains. The structural natures of the different crystalline phases are distinguished by the μ-LEED patterns in Figure 3G–J obtained from 250 nm diameter areas. The rotated *t*-BN layer shows Rh and rotated BN integer diffraction spots only. In the *m*-BN phase, the diffraction spots of the moiré lattice are visible and from the lower photoelectron yield of *m*-BN we infer a lower work function of *t*-BN (for details, see section S5.2 in the SI). Finally, the diffraction pattern of *d*-BN is reminiscent of *h*-BN/Rh(111) nanomesh with a commensurate 13 × 13 on 12 × 12 superstructure. The variation of the elastically scattered intensity along the surface normal versus incident electron energy in I(V) spectra gives rise to the energy dependence of bright field LEEM image contrast and also distinguishes various phases. The I(V) spectra of t_1-BN and t_2-BN in Figure

https://dx.doi.org/10.1021/acsnano.0c08616
ACS Nano 2021, 15, 1351–1357

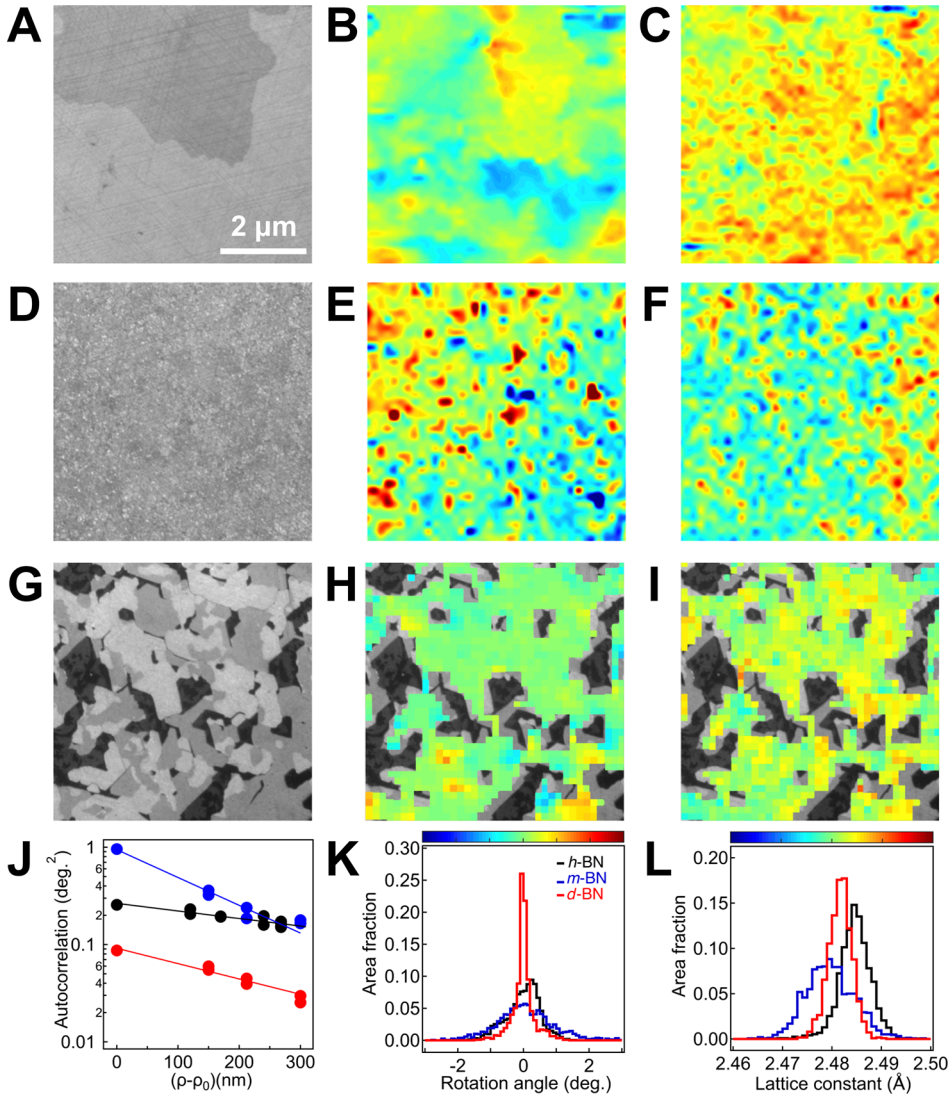

Figure 4. BN lattice properties from scanning μ-LEED at room temperature. (A–C) *h*-BN nanomesh grown on Rh(111) and annealed to 1210 K. (D–F) *m*-BN after annealing to 1100 K. (G–I) *d*-BN distilled from *m*-BN up to 1210 K. (A, D, G) LEEM bright field images. Color-coded (B, E, H) lattice rotation angles, α, and (C, F, I) lattice constants. (J–L) Characteristics of *h*-BN (black), *m*-BN (blue), and *d*-BN (red). (J) Spatial autocorrelation of lattice rotation angles. (K) Histogram of the lattice rotation angles. The average *m*-BN rotation angle of 24.3° is subtracted. (L) Histogram of the lattice constants.

3A are displayed in Figure 3K and show similar characteristics, while *m*-BN is distinctly different. The similarity of the I(V) spectra for t_1-BN and t_2-BN indicate that they have the same structure, but the higher intensity of t_2-BN means that it is cleaner. This cleaning process precedes the 2D distillation (see the video in the SI). Figure 3L displays the I(V) spectra for two different BN domains d_1-BN and d_2-BN in Figure 3F.

The *in situ* LEEM observations directly reveal the 2D distillation process, *i.e.*, the sublimation of BN onto the Rh(111) surface, the diffusion of these precursors, and condensation into a more stable material: *d*-BN. The residence-times of B and N on the surface are sufficiently long for this process to take place. Free *h*-BN fragments continue to be generated at the receding *m*-BN edge and diffuse toward the *d*-BN phase in response to the free energy difference between the *m*-BN and *d*-BN edges, respectively. This picture should be generally valid and applicable to the distillation growth of other 2D materials on Rh and other catalytic material surfaces used for CVD growth and transfer.

The *m*-BN → *d*-BN phase transformation is initiated at sparsely distributed defect sites (Figure S7). These defects are believed to be Rh particles bound to the underside of the transferred *h*-BN that were detached from the growth substrate during the transfer process. The areal density of the particles is in the order of 10^{-4} μm^{-2}. These point defects trigger the 2D distillation at low temperature, which is favorable for minimizing the loss of BN from the surface[19] and explain the circular shape of the phase transformation region. The choice of the catalyst surface plays an important role, as there is no evidence for 2D distillation in control experiments with *h*-BN on a SiO_2 surface (Figure S3).

In order to establish differences in the quality of *h*-BN nanomesh, *m*-BN and *d*-BN, lattice constants, lattice rotation angles, and mosaicities were determined quantitatively in submicron (250 nm) areas with high accuracy using μ-LEED. These characteristics are particularly relevant for the electronic performance of 2D materials. Figure 4 shows 6 × 6 μm^2 scanning μ-LEED images of a *h*-BN nanomesh, *m*-BN and *d*-

https://dx.doi.org/10.1021/acsnano.0c08616
ACS Nano 2021, 15, 1351–1357

BN. As for *d*-BN, *h*-BN may display in different domains as well, which explains the bright field contrast in Figure 4A, while such contrast is absent in the shown *m*-BN patch. The BN lattice rotation angles α and lattice constants a have been determined from more than 1000 different μ-LEED patterns recorded in the scan areas. The BN lattice constants of *d*-BN have the smallest scatter of 0.1%, while for *m*-BN it is about a factor of 2 larger. The average BN lattice rotation angle of *m*-BN is 24.3°, while *h*-BN and *d*-BN appear aligned to the Rh substrate. The mosaic spread or standard deviation of these angles is the smallest for *d*-BN. This is also reflected in the prefactors of the lateral autocorrelation of the rotation angles and we find the best correlation length λ_α of 560 nm for *h*-BN nanomesh, while it is 280 nm for *d*-BN and 150 nm for *m*-BN (see detailed analysis in S5.5 in the SI).

CONCLUSIONS

In summary, 2D distillation signifies gas-phase and precipitation induced growth as a way to synthesize 2D materials on surfaces. We investigated hexagonal boron nitride that is transferred back onto a rhodium substrate. Annealing of an arbitrarily oriented transferred single layer cleans the BN layer and leads to moiré interference with the substrate. Further annealing treatments lead to formation of *d*-BN by sublimation and recondensation with distinctly superior quality compared with the initially grown *h*-BN. Our results provide a method for fabricating high-quality *h*-BN monolayers without CVD setup. 2D distillation promises a synthesis route for any 2D material on catalytic substrates.

MATERIALS AND METHODS

CVD, Delamination, XPS, UPS, LEED, STM, and Raman Experiments. The *h*-BN monolayers are prepared with an ultrahigh vacuum (UHV) CVD method on 4-in. single-crystalline Rh(111) thin film wafers with a base pressure of 1×10^{-10} mbar.[37] For the 2 nm void generation with the "can-opener" effect, a Specs IQP 10/35 Penning-type ion source run at lowest acceleration potential was used.[24] The electrochemical delamination procedure of *h*-BN monolayer is described in detail in refs 18 and 19. XPS and UPS measurements were carried out in a VGESCALAB 220 system.[38] The STM experiments were performed in a variable-temperature scanning tunneling microscope (Omicron, VT-STM).[39]

LEEM Experiments. LEEM imaging and I(V) spectra measurements, conventional and scanning μ-LEED and PEEM were carried out in a noncommercial LEEM instrument.[36,40−42] PEEM measurements were performed using illumination from a mercury discharge lamp. Temperature was measured using an optical pyrometer with an emissivity setting of 0.1.

DFT Simulations. DFT simulations have been performed with the CP2K code[43] using the PBE-rVV10 density functional.[44−46] The ground-state calculations have been carried out under the Gaussian plane wave method and the molecular orbitals of the valence electrons are expanded into a combination of Gaussian and plane waves, whereas the core electrons are treated using Goedecker−Teter−Hutter pseudopotentials.[47] For the Gaussian basis set expansion, the valence orbitals have been expanded into molecularly optimized DZVP basis sets for all elements except Rh, where orbitals were expanded using a molecularly optimized SZVP basis.[48]

ASSOCIATED CONTENT

Supporting Information

The Supporting Information is available free of charge at https://pubs.acs.org/doi/10.1021/acsnano.0c08616.

XPS of back-transferred *h*-BN on Rh(111), STM of other moiré patterns, XPS and Raman analysis of back-transferred *h*-BN on SiO_2, DFT calculations, LEEM, PEEM and μ-LEED evaluations, including LEEM movie analysis, condensation seed, the $(2\sqrt{3} \times 2\sqrt{3})R30°$ superstructure, recording sites of μ-LEED and I(V) curves, and detailed μ-LEED evaluations (PDF)

LEEM movie (MP4)

AUTHOR INFORMATION

Corresponding Author

Huanyao Cun − *Physik-Institut, Universität Zürich, 8057 Zürich, Switzerland;* orcid.org/0000-0002-5225-9861; Email: hycun1@physik.uzh.ch

Authors

Zichun Miao − *Department of Physics, Hong Kong University of Science and Technology, Kowloon, Hong Kong SAR, China*

Adrian Hemmi − *Physik-Institut, Universität Zürich, 8057 Zürich, Switzerland*

Yasmine Al-Hamdani − *Department of Chemistry, University of Zürich, 8057 Zürich, Switzerland*

Marcella Iannuzzi − *Department of Chemistry, University of Zürich, 8057 Zürich, Switzerland;* orcid.org/0000-0001-9717-2527

Jürg Osterwalder − *Physik-Institut, Universität Zürich, 8057 Zürich, Switzerland;* orcid.org/0000-0001-9517-641X

Michael S. Altman − *Department of Physics, Hong Kong University of Science and Technology, Kowloon, Hong Kong SAR, China*

Thomas Greber − *Physik-Institut, Universität Zürich, 8057 Zürich, Switzerland;* orcid.org/0000-0002-5234-1937

Complete contact information is available at: https://pubs.acs.org/10.1021/acsnano.0c08616

Author Contributions

§H.C. and Z.M. contributed equally to this work.

Notes

The authors declare no competing financial interest.

ACKNOWLEDGMENTS

Financial support by the European Commission under the Graphene Flagship Core 2 (No. 785219) and the HKUST Block Grant DSCI17SC02 are gratefully acknowledged. We thank Mr. Michael Weinl and Dr. Matthias Schreck from Universität Augsburg, Germany for providing Rh metal substrates.

REFERENCES

(1) Geim, A. K.; Grigorieva, I. V. van der Waals Heterostructures. *Nature* **2013**, *499*, 419−425.

(2) Surwade, S. P.; Smirnov, S. N.; Vlassiouk, I. V.; Unocic, R. R.; Veith, G. M.; Dai, S.; Mahurin, S. M. Water Desalination Using Nanoporous Single-Layer Graphene. *Nat. Nanotechnol.* **2015**, *10*, 459−464.

(3) Cartamil-Bueno, S. J.; Cavalieri, M.; Wang, R.; Houri, S.; Hofmann, S.; van der Zant, H. S. J. Mechanical Characterization and Cleaning of CVD Single-Layer h-BN Resonators. *NPJ. 2D Mater. Appl.* **2017**, *1*, 1−7.

(4) Torrisi, F.; Hasan, T.; Wu, W.; Sun, Z.; Lombardo, A.; Kulmala, T. S.; Hsieh, G.-W.; Jung, S.; Bonaccorso, F.; Paul, P. J.; Chu, D.; Ferrari, A. C. Inkjet-Printed Graphene Electronics. *ACS Nano* **2012**, *6*, 2992−3006.

(5) Novoselov, K. S.; Geim, A. K.; Morozov, S. V.; Jiang, D.; Zhang, Y.; Dubonos, S. V.; Grigorieva, I. V.; Firsov, A. A. Electric Field Effect in Atomically Thin Carbon Films. *Science* **2004**, *306*, 666−669.
(6) Banszerus, L.; Schmitz, M.; Engels, S.; Dauber, J.; Oellers, M.; Haupt, F.; Watanabe, K.; Taniguchi, T.; Beschoten, B.; Stampfer, C. Ultrahigh-Mobility Graphene Devices from Chemical Vapor Deposition on Reusable Copper. *Sci. Adv.* **2015**, *1*, No. e1500222.
(7) Cao, Y.; Fatemi, V.; Fang, S.; Watanabe, K.; Taniguchi, T.; Kaxiras, E.; Jarillo-Herrero, P. Unconventional Superconductivity in Magic-Angle Graphene Superlattices. *Nature* **2018**, *556*, 43−50.
(8) Dean, C. R.; Young, A. F.; Meric, I.; Lee, C.; Wang, L.; Sorgenfrei, S.; Watanabe, K.; Taniguchi, T.; Kim, P.; Shepard, K. L.; Hone, J. Boron Nitride Substrates for High-Quality Graphene Electronics. *Nat. Nanotechnol.* **2010**, *5*, 722−726.
(9) Nagashima, A.; Tejima, N.; Gamou, Y.; Kawai, T.; Oshima, C. Electronic Structure of Monolayer Hexagonal Boron Nitride Physisorbed on Metal Surfaces. *Phys. Rev. Lett.* **1995**, *75*, 3918−3921.
(10) Corso, M.; Auwärter, W.; Muntwiler, M.; Tamai, A.; Greber, T.; Osterwalder, J. Boron Nitride Nanomesh. *Science* **2004**, *303*, 217−220.
(11) Farwick zum Hagen, F. H.; Zimmermann, D. M.; Silva, C. C.; Schlueter, C.; Atodiresei, N.; Jolie, W.; Martínez-Galera, A. J.; Dombrowski, D.; Schröder, U. A.; Will, M.; Lazić, P.; Caciuc, V.; Blügel, S.; Lee, T.-L.; Michely, T.; Busse, C. Structure and Growth of Hexagonal Boron Nitride on Ir(111). *ACS Nano* **2016**, *10*, 11012−11026.
(12) Lee, J. S.; Choi, S. H.; Yun, S. J.; Kim, Y. I.; Boandoh, S.; Park, J.-H.; Shin, B. G.; Ko, H.; Lee, S. H.; Kim, Y.-M.; Lee, Y. H.; Kim, K. K.; Kim, S. M. Wafer-Scale Single-Crystal Hexagonal Boron Nitride Film *via* Self-Collimated Grain Formation. *Science* **2018**, *362*, 817−821.
(13) Wang, L.; Xu, X.; Zhang, L.; Qiao, R.; Wu, M.; Wang, Z.; Zhang, S.; Liang, J.; Zhang, Z.; Zhang, Z.; Chen, W.; Xie, X.; Zong, J.; Shan, Y.; Guo, Y.; Willinger, M.; Wu, H.; Li, Q.; Wang, W.; Gao, P.; et al. Epitaxial Growth of a 100-Square-Centimetre Single-Crystal Hexagonal Boron Nitride Monolayer on Copper. *Nature* **2019**, *570*, 91−95.
(14) Chen, T.-A.; Chuu, C.-P.; Tseng, C.-C.; Wen, C.-K.; Wong, H. S. P.; Pan, S.; Li, R.; Chao, T.-A.; Chueh, W.-C.; Zhang, Y.; Fu, Q.; Yakobson, B. I.; Chang, W.-H.; Li, L.-J. Wafer-Scale Single-Crystal Hexagonal Boron Nitride Monolayers on Cu(111). *Nature* **2020**, *579*, 219−223.
(15) Suzuki, S.; Pallares, R. M.; Hibino, H. Growth of Atomically Thin Hexagonal Boron Nitride Films by Diffusion through a Metal Film and Precipitation. *J. Phys. D: Appl. Phys.* **2012**, *45*, 385304.
(16) Zhang, C.; Fu, L.; Zhao, S.; Zhou, Y.; Peng, H.; Liu, Z. Controllable Co-Segregation Synthesis of Wafer-Scale Hexagonal Boron Nitride Thin Films. *Adv. Mater.* **2014**, *26*, 1776−1781.
(17) Auwaerter, W. Hexagonal Boron Nitride Monolayers on Metal Supports: Versatile Templates for Atoms, Molecules and Nanostructures. *Surf. Sci. Rep.* **2019**, *74*, 1−95.
(18) Cun, H. Y.; Hemmi, A.; Miniussi, E.; Bernard, C.; Probst, B.; Liu, K.; Alexander, D. T. L.; Kleibert, A.; Mette, G.; Weinl, M.; Schreck, M.; Osterwalder, J.; Radenovic, A.; Greber, T. Centimeter-Sized Single-Orientation Monolayer Hexagonal Boron Nitride with or without Nanovoids. *Nano Lett.* **2018**, *18*, 1205−1212.
(19) Hemmi, A.; Cun, H. Y.; Tocci, G.; Epprecht, A.; Stel, B.; Lingenfelder, M.; de Lima, L. H.; Muntwiler, M.; Osterwalder, J.; Iannuzzi, M.; Greber, T. Catalyst Proximity-Induced Functionalization of h-BN with Quat Derivatives. *Nano Lett.* **2019**, *19*, 5998−6004.
(20) Berner, S.; Corso, M.; Widmer, R.; Groening, O.; Laskowski, R.; Blaha, P.; Schwarz, K.; Goriachko, A.; Over, H.; Gsell, S.; Schreck, M.; Sachdev, H.; Greber, T.; Osterwalder, J. Boron Nitride Nanomesh: Functionality from a Corrugated Monolayer. *Angew. Chem., Int. Ed.* **2007**, *46*, 5115−5119.
(21) Gsell, S.; Fischer, M.; Schreck, M.; Stritzker, B. Epitaxial Films of Metals from the Platinum Group (Ir, Rh, Pt and Ru) on YSZ-Buffered Si(111). *J. Cryst. Growth* **2009**, *311*, 3731−3736.
(22) Goriachko, A.; He; Knapp, M.; Over, H.; Corso, M.; Brugger, T.; Berner, S.; Osterwalder, J.; Greber, T. Self-Assembly of a Hexagonal Boron Nitride Nanomesh on Ru(0001). *Langmuir* **2007**, *23*, 2928−2931.
(23) Morscher, M.; Osterwalder, J.; Greber, T. Formation of Single Layer h-BN on Pd(111). *Surf. Sci.* **2006**, *600*, 3280−3284.
(24) Cun, H. Y.; Iannuzzi, M.; Hemmi, A.; Roth, S.; Osterwalder, J.; Greber, T. Immobilizing Individual Atoms beneath a Corrugated Single Layer of Boron Nitride. *Nano Lett.* **2013**, *13*, 2098−2103.
(25) Cun, H. Y.; Iannuzzi, M.; Hemmi, A.; Osterwalder, J.; Greber, T. Two-Nanometer Voids in Single-Layer Hexagonal Boron Nitride: Formation *via* the "Can-Opener" Effect and Annihilation by Self-Healing. *ACS Nano* **2014**, *8*, 7423−7431.
(26) Hermann, K. Periodic Overlayers and Moire Patterns: Theoretical Studies of Geometric Properties. *J. Phys.: Condens. Matter* **2012**, *24*, 314210.
(27) Dil, H.; Lobo-Checa, J.; Laskowski, R.; Blaha, P.; Berner, S.; Osterwalder, J.; Greber, T. Surface Trapping of Atoms and Molecules with Dipole Rings. *Science* **2008**, *319*, 1824−1826.
(28) Iannuzzi, M.; Tran, F.; Widmer, R.; Dienel, T.; Radican, K.; Ding, Y.; Hutter, J.; Gröning, O. Site-Selective Adsorption of Phthalocyanine on h-BN/Rh(111) Nanomesh. *Phys. Chem. Chem. Phys.* **2014**, *16*, 12374−12384.
(29) Huang, M.; Yan, H.; Chen, C.; Song, D.; Heinz, T.; Hone, J. Phonon Softening and Crystallographic Orientation of Strained Graphene Studied by Raman Spectroscopy. *Proc. Natl. Acad. Sci. U. S. A.* **2009**, *106*, 7304−7308.
(30) Couto, N. J. G.; Costanzo, D.; Engels, S.; Ki, D.-K.; Watanabe, K.; Taniguchi, T.; Stampfer, C.; Guinea, F.; Morpurgo, A. F. Random Strain Fluctuations as Dominant Disorder Source for High-Quality On-Substrate Graphene Devices. *Phys. Rev. X* **2014**, *4*, 041019.
(31) Sutter, P. W.; Flege, J.-I.; Sutter, E. A. Epitaxial Graphene on Ruthenium. *Nat. Mater.* **2008**, *7*, 406−411.
(32) Man, K. L.; Altman, M. S. Low Energy Electron Microscopy and Photoemission Electron Microscopy Investigation of Graphene. *J. Phys: Condens. Matt.* **2012**, *24*, 314209.
(33) Mende, P.; Gao, Q.; Ismach, A.; Chou, H.; Widom, M.; Ruoff, R.; Colombo, L.; Feenstra, R. Characterization of Hexagonal Boron Nitride Layers on Nickel Surfaces by Low-Energy Electron Microscopy. *Surf. Sci.* **2017**, *659*, 31−42.
(34) Petrovic, M.; Hagemann, U.; Horn-von Hoegen, M.; zu Heringdorf, F.-J. M. Microanalysis of Single-Layer Hexagonal Boron Nitride Islands on Ir(111). *Appl. Surf. Sci.* **2017**, *420*, 504−510.
(35) Felter, J.; Raths, M.; Franke, M.; Kumpf, C. *In Situ* Study of Two-Dimensional Dendritic Growth of Hexagonal Boron Nitride. *2D Mater.* **2019**, *6*, 045005.
(36) Man, K. L.; Altman, M. S. Small-Angle Lattice Rotations in Graphene on Ru(0001). *Phys. Rev. B: Condens. Matter Mater. Phys.* **2011**, *84*, 235415.
(37) Hemmi, A.; Bernard, C.; Cun, H. Y.; Roth, S.; Klöckner, M.; Kälin, T.; Weinl, M.; Gsell, S.; Schreck, M.; Osterwalder, J.; Greber, T. High Quality Single Atomic Layer Deposition of Hexagonal Boron Nitride on Single Crystalline Rh(111) Four-Inch Wafers. *Rev. Sci. Instrum.* **2014**, *85*, 035101.
(38) Greber, T.; Raetzo, O.; Kreutz, T. J.; Schwaller, P.; Deichmann, W.; Wetli, E.; Osterwalder, J. A Photoelectron Spectrometer for K-Space Mapping above the Fermi Level. *Rev. Sci. Instrum.* **1997**, *68*, 4549−4554.
(39) Ma, H.; Brugger, T.; Berner, S.; Ding, Y.; Iannuzzi, M.; Hutter, J.; Osterwalder, J.; Greber, T. Nano-Ice on Boron Nitride Nanomesh: Accessing Proton Disorder. *ChemPhysChem* **2010**, *11*, 399−403.
(40) Altman, M. S. Trends in Low Energy Electron Microscopy. *J. Phys.: Condens. Matter* **2010**, *22*, 084017.
(41) Bauer, E. *Surface Microscopy with Low Energy Electrons*; Springer: New York, 2014.
(42) Yu, K. M.; Lau, K. L. W.; Altman, M. S. Fourier Optics of Image Formation in Aberration-Corrected LEEM. *Ultramicroscopy* **2019**, *200*, 160−168.

https://dx.doi.org/10.1021/acsnano.0c08616
ACS Nano 2021, 15, 1351−1357

(43) Hutter, J.; Iannuzzi, M.; Schiffmann, F.; VandeVondele, J. Cp2k: Atomistic Simulations of Condensed Matter Systems. *Wiley Interdiscip. Rev.: Comput. Mol. Sci.* **2014**, *4*, 15−25.
(44) Perdew, J. P.; Burke, K.; Ernzerhof, M. Generalized Gradient Approximation Made Simple. *Phys. Rev. Lett.* **1996**, *77*, 3865−3868.
(45) Vydrov, O. A.; Van Voorhis, T. Nonlocal van der Waals Density Functional Made Simple. *Phys. Rev. Lett.* **2009**, *103*, 63004−63007.
(46) Sabatini, R.; Gorni, T.; de Gironcoli, S. Nonlocal van der Waals Density Functional Made Simple and Efficient. *Phys. Rev. B: Condens. Matter Mater. Phys.* **2013**, *87*, 41108−41111.
(47) Goedecker, S.; Teter, M.; Hutter, J. Separable Dual-Space Gaussian Pseudopotentials. *Phys. Rev. B: Condens. Matter Mater. Phys.* **1996**, *54*, 1703−1710.
(48) VandeVondele, J.; Hutter, J. Gaussian Basis Sets for Accurate Calculations on Molecular Systems in Gas and Condensed Phases. *J. Chem. Phys.* **2007**, *127*, 114105.

https://dx.doi.org/10.1021/acsnano.0c08616
ACS Nano 2021, 15, 1351−1357

Supporting Information: High-Quality Hexagonal Boron Nitride from 2D Distillation

Huanyao Cun,[*,†,§] Zichun Miao,[‡,§] Adrian Hemmi,[†] Yasmine Al-Hamdani,[¶] Marcella Iannuzzi,[¶] Jürg Osterwalder,[†] Michael S. Altman,[‡] and Thomas Greber[†]

†*Physik-Institut, Universität Zürich, Winterthurerstrasse 190, 8057 Zürich, Switzerland*

‡*Department of Physics, Hong Kong University of Science and Technology, Kowloon, Hong Kong, China*

¶*Department of Chemistry, University of Zürich, 8057 Zürich, Switzerland*

§*Contributed equally to this work*

E-mail: hycun1@physik.uzh.ch

Contents

1 XPS of Back-Transferred h-BN on Rh(111)

After h-BN delamination, the Rh(111) substrates were analyzed by X-ray photoelectron spectroscopy (XPS) and low-energy electron diffraction (LEED), which confirm the Rh(111)

substrate to be h-BN free.[S1] After back-transfer of h-BN on other Rh(111) substrates, XPS and LEED measurements were carried out as well. Fig. S1 displays the corresponding XPS results. For comparison to pristine h-BN/Rh(111) nanomesh samples before delamination, transfer rates above 95% were inferred.

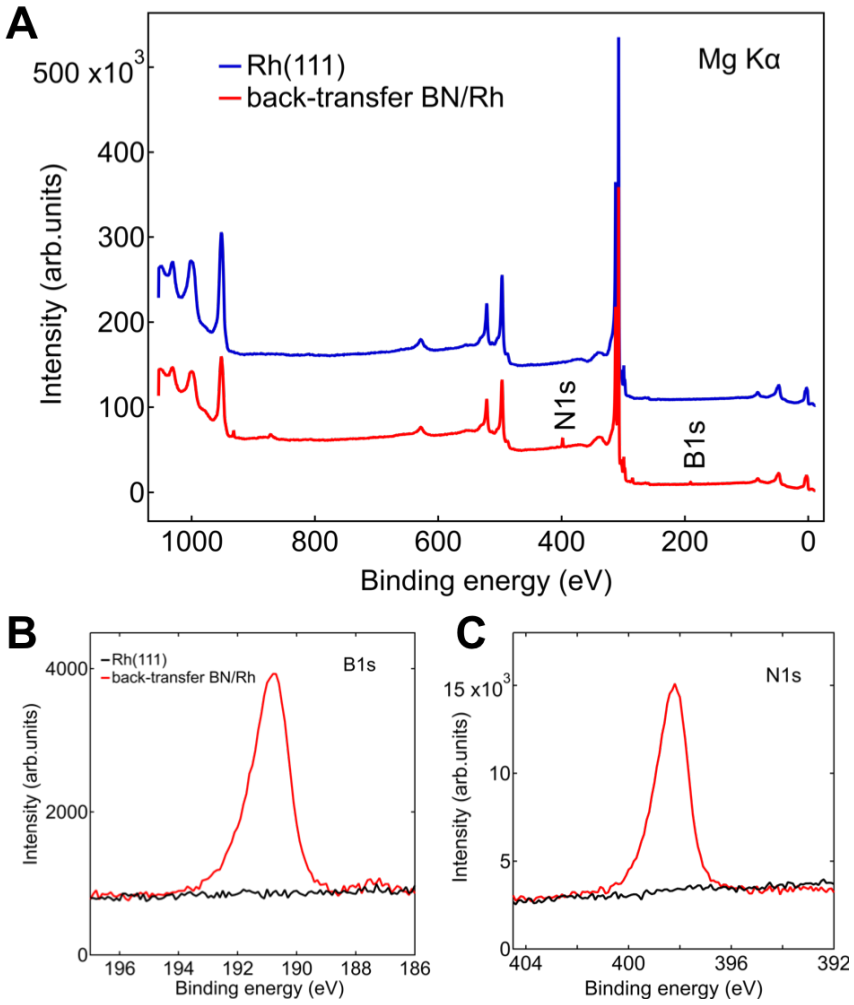

Figure S1: **XPS of back-transferred h-BN on Rh(111).** (A) XPS (MgKα, $\hbar\omega = 1253.6$ eV) survey spectra of Rh(111) after h-BN monolayer delamination (blue), and after back-transferred h-BN (red) on Rh(111). (B & C) B1s and N1s spectra of the Rh(111) substrates after delamination (black) and after back-transfer of h-BN (red).

2 STM of Other Moiré Patterns of Back-transferred *h*-BN on Rh(111)

After annealing back-transferred *h*-BN on Rh(111) to 750 K, scanning tunnelling microscopy (STM) measurements were carried out at room temperature. Besides the moiré patterns displayed in Fig. 1C of the main text, other moiré patterns are observed as well. Fig. S2 shows two more representative moiré superstructures.

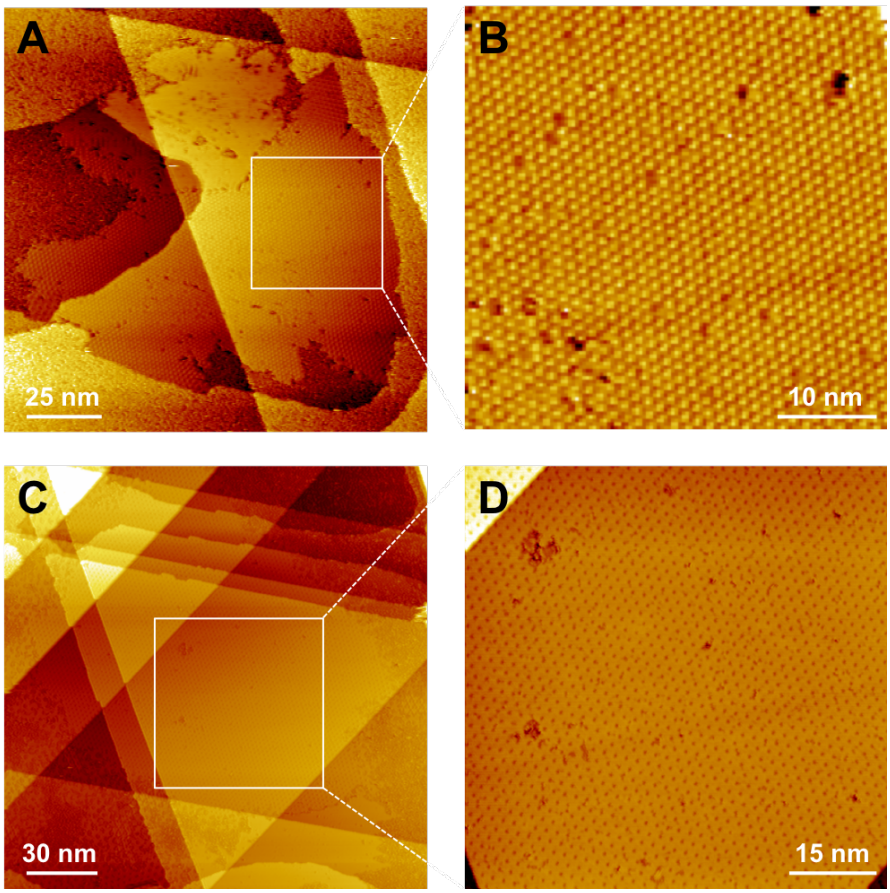

Figure S2: **Different moiré superstructures of back-transferred *h*-BN on Rh(111) after annealing.** (A & C) Large-area STM images of back-transferred BN on Rh(111) after annealing to 750 K. Ordered superstructures and "messy" areas are observed. (B & D) are two zoom-ins marked as white squares in (A) and in (C). Here the moiré superstructure lattice constants are 1.5 nm (B) and 2.2 nm (D). U = -1.20 V, I = 0.50 nA.

3 XPS and Raman Analysis of Back-transferred *h*-BN on SiO_2

In order to pinpoint the importance of the Rh catalyst substrate for back-transfer and annealing effects, *h*-BN was transferred on SiO_2 substrates. Systematic cycles of annealing were carried out from 500°C to 900°C and followed with XPS measurement after each annealing step. In this temperature interval the stoichiometry of the surface remains constant. *Ex-situ* Raman measurements are recorded before and after the annealing cycles and indicate no quality improvement of *h*-BN/SiO_2 that was annealed to 900°C, while the same temperature treatment for BN layers on catalytic substrates show a significant quality enhancement of the *h*-BN nanomesh.

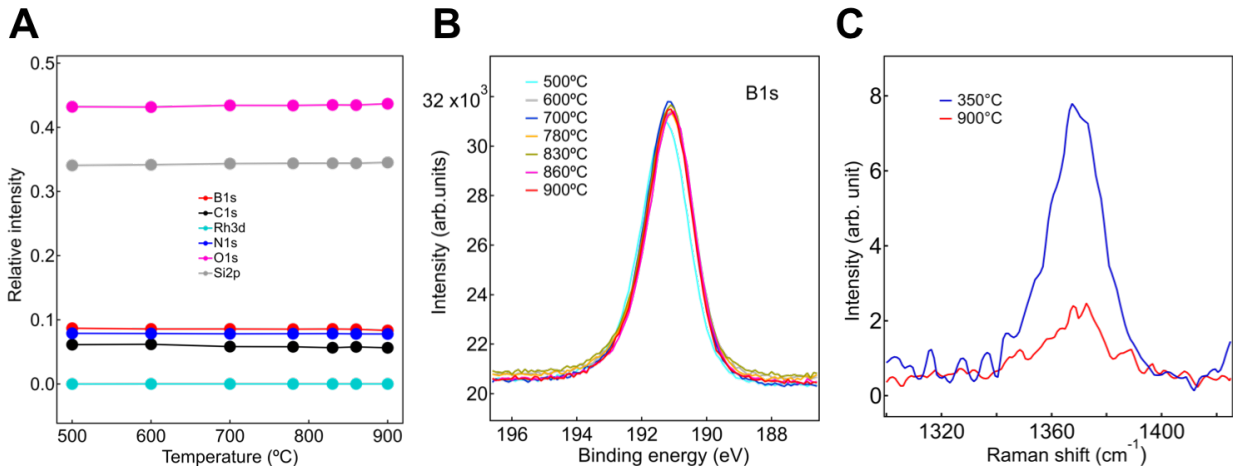

Figure S3: **Back-transferred *h*-BN on SiO_2.** (A & B) XPS results of a series of annealing cycles. (A) Elemental abundance of the 6 investigated elements after different annealing cycles between 500°C and 900°C: B1s (red), N1s (blue), C1s (black), Rh3d (cyan-blue), O1s (pink) and Si2p (grey). (B) B1s core level peak after the different annealing cycles. (C) Raman spectra before (blue) and after (red) high temperature annealing (900°C).

4 DFT Calculations

4.1 The Commensurate 19 on 16 Moiré Structure

Density functional theory (DFT) calculations confirm that *h*-BN can adsorb on Rh with different orientations, *i.e.*, forming different moiré patterns. We have optimised a supercell with 19 *h*-BN units on top of 16 Rh(111) units, where the BN hexagonal lattice is rotated by 23.4 degrees with respect to the fcc(111) lattice of the substrate, and where the BN areal density is very similar, *i.e.*, 1% larger than for the well-known *h*-BN/Rh(111) nanomesh. The relaxed atomic structure is shown in Figure S4. It presents one anchoring point where the N corner atom on top of a surface Rh atom binds to the metal (N-Rh = 2.35 Å). At this anchor site the *h*-BN bends towards the metal but remains otherwise rather flat at a height between 3 and 3.3 Å from the surface. The adsorption energy per BN pair is -0.164 eV, *i.e.*, less than the adsorption energy computed for the 169 BN on 144 Rh units (nanomesh), which at the same level of theory is -0.20 eV per BN pair.[S2,S3]

The corrugation of the *h*-BN layer corresponds to a modulation of the electronic structure, as it has been observed for the *h*-BN nanomesh. In particular, we distinguish the presence of the binding N atoms in both, the red shift of the N1s states, as well as the shift of the Np_x and Np_y bands in the projected density of states. In Figure S5 the N1s and Np_{xy} valence band density of states as computed for the 19 on 16 R=23.4° moiré and the nanomesh, are compared. For the 19 on 16 structure the σ-states assigned to the corner atom ($\sigma_{\beta'}$ in the experiment in Fig. 2) have a higher energy than the pore states in the *h*-BN nanomesh (σ_{β} in the experiment in Fig. 2) and the shift of the gravity center of the p_{xy} states between the corner and the rest is as well smaller than that between the pore and the wire in the *h*-BN nanomesh. This is in agreement with the photoemission experiments.

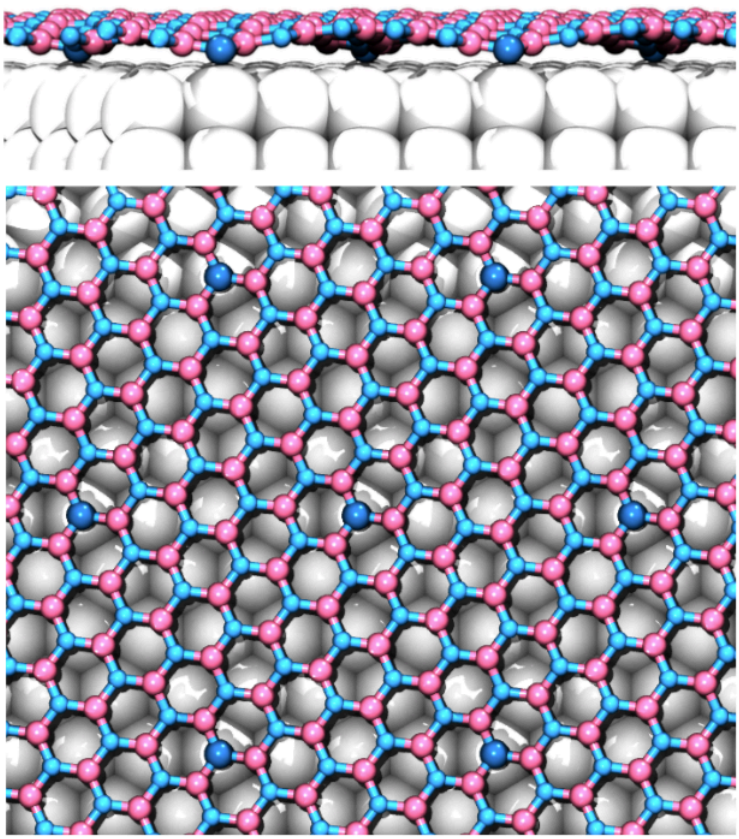

Figure S4: **DFT coordinates of the 19 h-BN on 16 Rh(111) R23.4 ° structure.** Top: side view, bottom: top view. Color codes: Rhodium-grey, nitrogen-blue and boron-pink. The nitrogen corner atom at the anchoring site is depicted dark blue and bigger.

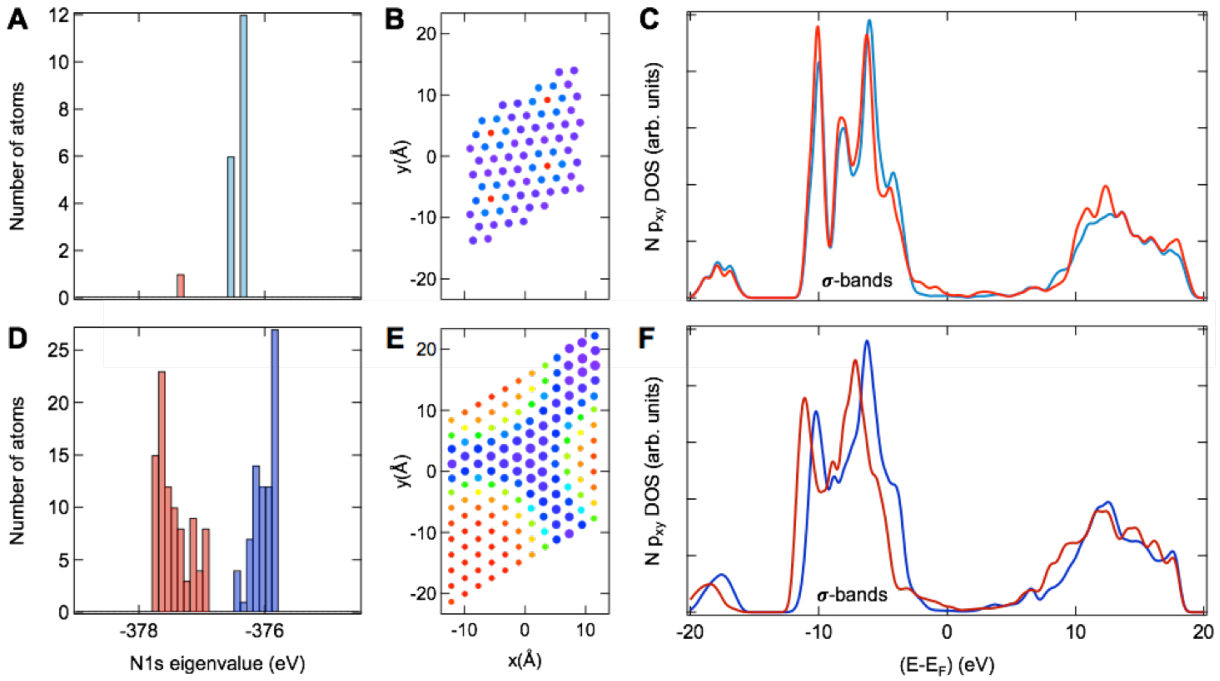

Figure S5: **DFT results on the 19 on 16 and the 169 on 144 BN on Rh(111) structures**. (A) The N1s eigenvalues separate the 19 nitrogen atoms into two distinct groups, where the value with the lowest energy can be assigned to the N corner atom that binds on top of a Rh atom at the anchoring site. The group of 6 nitrogen atoms belongs to the BN unit cells neighbouring the corner atom, and the remaining 12 to the rest of the super cell. (B) the in-plane x-y coordinates of four 19 on 16 unit cells are shown. The color code represents the N1s eigenvalues in (A) and the radius of the circular markers the height of the N atoms above the Rh substrate. (C) Atomic p_{xy} density of states on the two groups of nitrogen atoms as they are distinguished from (A) (corner atom-red, rest of the atoms-blue). The gravity center of the sigma band of the corner atom lies at -7.54 eV, and 0.31 eV below that of weakly bound atoms. The eigenvalues with the corresponding p_{xy} weight were convoluted with a Gaussian with 0.75 eV full width half maximum. (D-F) same as (A-C) for the 169 nitrogen atoms in the *h*-BN/Rh(111) nanomesh where the gravity center of the sigma band of the 92 strongly bonding atoms lies at -7.99 eV, and 0.87 eV below that of the nitrogen on the wires. (pore atoms-red, wire atoms-blue).

4.2 Adsorption Energies of B, C, N and O on Rh(111)

Density functional theory (DFT) calculations confirm that elemental boron binds stronger than elemental nitrogen on Rh(111). We have optimised the the geometries of elemental B, C, N and O in a Rh(111)(2×2) unit cell (see Table S1). The calculations were performed at the Gamma point and we used a slab of 6 layers of Rh separated by 39 Å vacuum. The

single atoms and the bare substrate were computed in the same unit cell as the slab and the adsorption energies are corrected for the basis set superposition error. The exchange-correlation functional PBE+D3 (including the three-body ATM term) and CP2K version 7.0 was used. The results for C, N and O agree well with existing calculations of Mavrikakis *et al.*[S4]

Table S1: Adsorption sites and binding energies of boron, carbon, nitrogen and oxygen atoms on Rh(111) as obtained by density functional theory.

element	adsorption site	adsorption energy (eV)
B	hcp	-6.17
C	hcp	-7.17
N	hcp	-5.20
O	fcc	-4.81

5 LEEM, PEEM and μ-LEED

Low energy electron microscopy (LEEM) and photoemission electron microscope (PEEM) were used to study the kinetics of 2D distillation, the related surface structures and their morphologies.

5.1 LEEM Movie

Movie legend(Movie S1, MP4 format): Transformation from t-BN to m-BN and then to d-BN. The LEEM video shows the annealing sequence displayed in Fig. 3 of the main text. The duration of the movie of 43 s covers 48 minutes real-time of the experiment. The sample temperature changes from 853°C to 937°C. The field of view (FOV) is 23 μm.

Phase Evolution from t-BN to d-BN

Fig. S6 shows the evolution of the areal weight of the different phases in the field of view (FOV=23 μm) of the movie and the sample temperature during the experiment. The temperatures and time of the four zoom-ins in Fig. 3B-3E and Fig. 3A&3F are marked with

circles. The grey overlays indicate the time intervals that were not shown in the movie due to thermal drift and readjustments of the electron microscope.

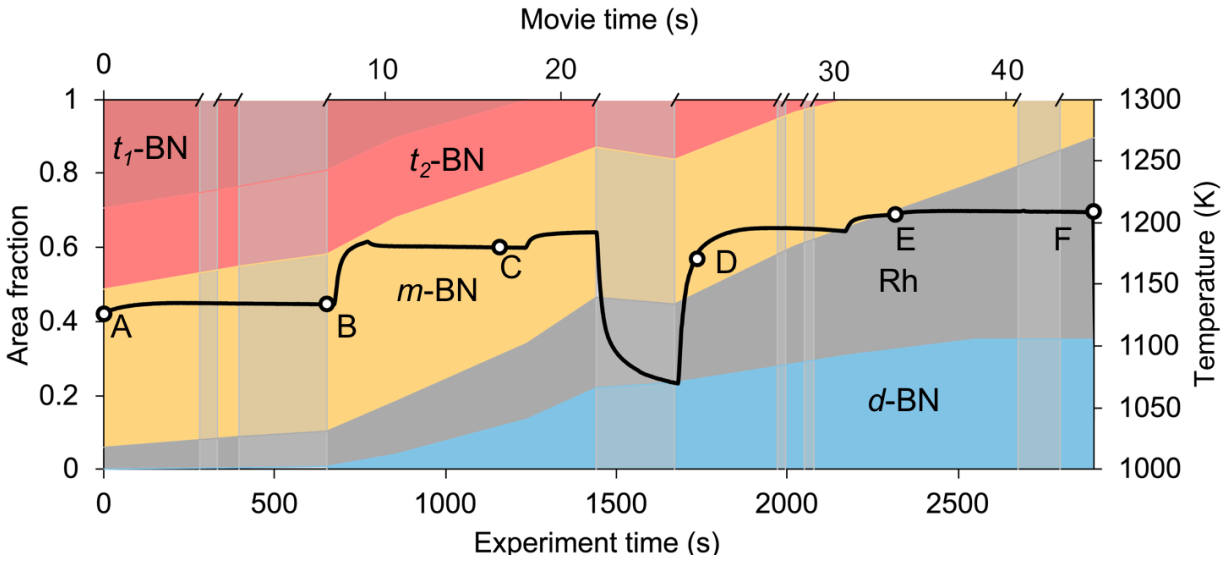

Figure S6: **Phase evolution during the LEEM movie.** Fraction of the different phases t_1-BN (dark red), t_2-BN (red), m-BN (yellow), Rh (grey) and d-BN (blue) during the movie recording. The sample temperature is indicated with a black line. The circles A, B, C, D, E & F mark temperatures and times of Fig. 3A&3F and the four zoom-ins in Figs. 3B-3E. The grey overlays indicate time intervals that are not shown in the movie, and correspondingly alter the relation between the Experiment time and the Movie time.

5.2 Condensation Seed

Figure S7 provides an overview of the growth fronts with a zoom-out LEEM bright field image after the 2D distillation growth of d-BN depicted in the movie (Sec. 5.1). In the center of the circular reaction site a catalytic particle is spotted around which d-BN condenses. The data are recorded at room temperature after annealing to 937°C. Furthermore a PEEM image of the same region is shown. The significant contrast in electron yield indicates that t-BN has the lowest work function of the different BN phases. Furthermore, the weak contrast between the m-BN and d-BN and the exposed Rh surface indicates that Rh has the highest work function.

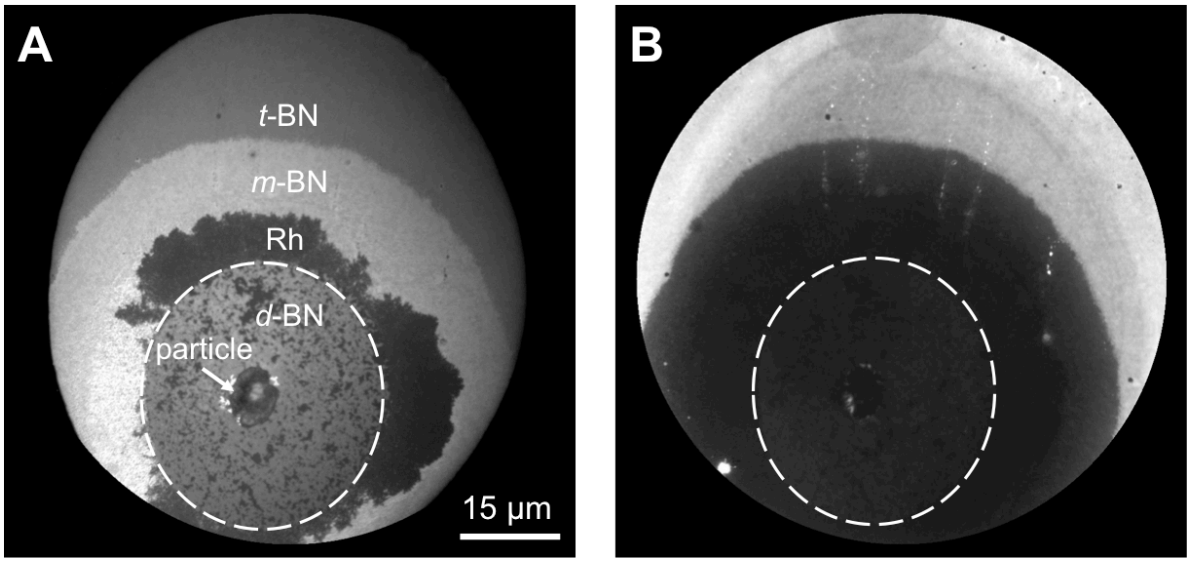

Figure S7: **LEEM and PEEM of the circular reaction site.** (A) Bight field LEEM image (E = 15 eV) of the BN-layer after 2D distillation growth at 937°C. d-BN growth emanates from a catalytic particle. It is surrounded concentrically by bare Rh, m-BN and t-BN. (B) A PEEM image formed using UV excitation from a Hg arc lamp is shown in the same location. Photoelectron yield contrast in this image originates in work function differences between the BN phases and the bare Rh substrate.

5.3 The $(2\sqrt{3} \times 2\sqrt{3})$R30° Superstructure

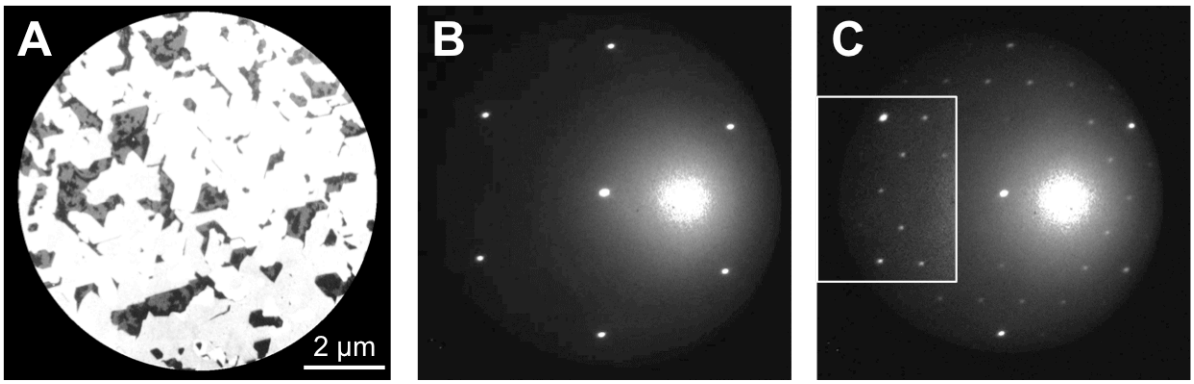

Figure S8: **Superstructures.** (A) A contrast enhanced version of the bright field LEEM image (E=15.0 eV) of d-BN presented in Fig. 4G reveals two phases on the Rh substrate. The bright and dark regions on the exposed Rh surface in (A) exhibit Rh(111) (1×1) (B) and $(2\sqrt{3} \times 2\sqrt{3})$R30° superstructure μ-LEED patterns (C). The area enclosed in the white bordered rectangle in (C) was contrast enhanced.

5.4 Recording Sites of μ-LEED and I(V) Spectra

Figure S9 shows the positions where the μ-LEED patterns and the I(V) spectra shown in Fig. 3 were recorded at room temperature: (A) before and (B) after the distillation growth shown in the movie.

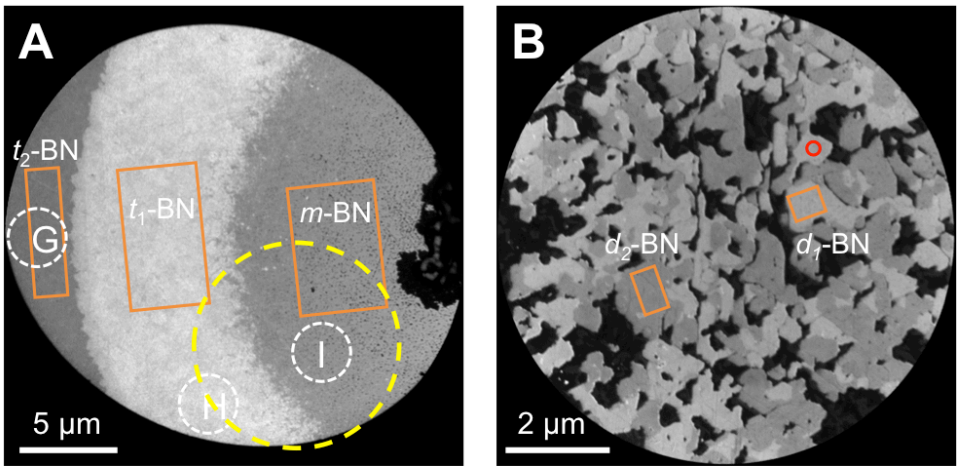

Figure S9: **Positions of the μ-LEED patterns and I(V) spectra measurements in Fig. 3 of the main text.** (A) LEEM image (E=12 eV) after annealing to 1100 K. (B) LEEM image (E=15 eV) after annealing to 1210 K. The yellow dashed circle indicates the zoom-in area shown in Figs. 3B-3E. The orange boxes indicate the area where the I(V) spectra for t_1-BN, t_2-BN, m-BN, d_1-BN and d_2-BN presented in Fig. 3K and Fig. 3L were measured. The white dashed circles indicate the 3 micro diameter areas where the μ-LEED patterns in Figs. 3G-3I were measured. The red solid circle indicates the 250 nm diameter area where the μ-LEED pattern in Fig. 3J was measured.

5.5 μ-LEED Evaluations

Rh Reference Data

As a reference for the absolute lattice constants the Rh(1x1) substrate lattice constant of 3.8031 Å that translates into a nearest neighbour distance of 2.689 Å[S5] has been used.

μ-LEED Spot Position Analysis

BN Lattice rotations and lattice constants as quoted in Table S2 are determined from the azimuthal and radial positions of superstructure or integer-order diffraction spots in μ-LEED

patterns measured in 250 nm diameter areas. Azimuthal positions are measured with respect to the 6-fold symmetric positions at 60° intervals of an ideal lattice that is aligned with the Rh substrate. Radial positions are measured from the (00) beam position at the center of the μ-LEED pattern. The inverse length scale of the pattern is calibrated by radial positions of Rh substrate integer-order spot positions. Spot-profile analysis (SPA) software is used to extract the diffraction peak positions. The SPA software determines peak positions very precisely by Gaussian fitting of the diffraction spot profile. The resolution of this determination is better than the scale set by the diffraction spot width. The results obtained for every μ-LEED pattern recorded in a 40×40 scan array are used to determine the BN lattice rotation angle α with respect to the substrate and lattice constant a at each local position probed by the beam in the scan area. These data are used to generate the μ-LEED images shown in Figs. 4B, 4C, 4E, 4F, 4H and 4I in the main text. Histograms of the values of lattice constant and rotation angle are prepared as shown in Figs. 4K and 4L in the main text. In the analysis of rotation angle, $\alpha = 0$ is the azimuthal orientation of an ideal BN lattice aligned with the substrate. The values of α and a in table S1 are the average values and the rotatioal mosaic $\Delta\alpha$ and lattice constant variation Δa in table S1 are the stand deviations of the distributions.

The Correlation Length λ_α

In order to further characterize the quality of the layers we perform an autocorrelation analysis of the mosaic angles. The autocorrelation tells on how related the signals in two pixels at distance $\rho - \rho_0 = \sqrt{\Delta x^2 + \Delta y^2}$ are. For the pixel maps with signal $\alpha(x, y)$ we find for the spacial autocorrelation:

$$R_{\alpha,\alpha}(\rho - \rho_0) = \frac{1}{N} \sum_{i=1}^{N} \alpha_i(\rho)\alpha_i(\rho_0) \tag{1}$$

where N is the number of pixels in the image and whenever $\rho - \rho_0$ falls outside the set of pixels $\alpha_i(\rho)\alpha_i(\rho_0)$ is set zero. If the average of a dataset is zero, $R_{\alpha,\alpha}(0)$ is the variance

σ^2. For white noise $R_{\alpha,\alpha}(0)$ drops to zero for $(\rho - \rho_0) > 0$ because there is no correlation between different pixels. If there is a correlation between neighbouring pixels that decays exponentially we get:

$$R_{\alpha,\alpha}(\rho - \rho_0) = \sigma^2 \exp(-(\rho - \rho_0)/\lambda_\alpha) \tag{2}$$

where the decay length λ_α is a characteristic length-scale that is extracted from the datasets of the angular orientation, and where for the case of m-BN the average rotation angle α has been subtracted.

Summary of Parameters Extracted from the Data in Fig. 4

Table S2 shows the structural parameters extracted from the μ-LEED data in Fig. 4, and the Rh substrate. The variance σ^2 as obtained from the autocorrelation (Eq. 1) for $\rho - \rho_0 = 0$ and confirms that $\Delta\alpha = \sigma$.

Table S2: Parameters as obtained for the μ-LEED data in Fig. 4 and the Rh(1x1) substrate. The lattice orientation α of Rh and the lattice constant a of Rh are taken as reference.[S5] The rotational mosaic $\Delta\alpha$ and the lattice constant variation Δa are the standard deviations of the observed distributions for the given phases. λ_α is the lateral correlation length of the the lattice orientation. σ^2 is the autocorrelation value $R_{\alpha,\alpha}(0)$, *i.e.*, variance of the datasets.

phase	α(deg.)	$\Delta\alpha$(deg.)	a(Å)	Δa(Å)	λ_α(nm)	σ^2(deg.^{2})
h-BN	0.00	0.51	2.485	0.0033	563	0.264
m-BN	24.28	0.98	2.480	0.0049	152	0.944
d-BN	0.00	**0.33**	**2.482**	**0.0024**	**276**	**0.094**
Rh	**0**	0.05	**2.689**	0.0022	-	-

References

(S1) Cun, H. Y.; Hemmi, A.; Miniussi, E.; Bernard, C.; Probst, B.; Liu, K.; Alexander, D. T. L.; Kleibert, A.; Mette, G.; Weinl, M.; Schreck, M.; Osterwalder, J.; Radenovic, A.; Greber, T. Centimeter-Sized Single-Orientation Monolayer Hexagonal Boron Nitride with or without Nanovoids. *Nano Lett.* **2018**, *18*, 1205–1212.

(S2) Iannuzzi, M.; Tran, F.; Widmer, R.; Dienel, T.; Radican, K.; Ding, Y.; Hutter, J.; Gröning, O. Site-Selective Adsorption of Phthalocyanine on h-BN/Rh(111) Nanomesh. *Phys. Chem. Chem. Phys.* **2014**, *16*, 12374–12384.

(S3) Hemmi, A.; Cun, H. Y.; Tocci, G.; Epprecht, A.; Stel, B.; Lingenfelder, M.; de Lima, L. H.; Muntwiler, M.; Osterwalder, J.; Iannuzzi, M.; Greber, T. Catalyst Proximity-Induced Functionalization of h-BN with Quat Derivatives. *Nano Lett.* **2019**, *19*, 5998–6004.

(S4) Mavrikakis, M.; Rempel, J.; Greeley, J.; Hansen, L. B.; N¿rskov, J. K. Atomic and Molecular Adsorption on Rh(111). *The Journal of Chemical Physics* **2002**, *117*, 6737–6744.

(S5) Zemann, J. Crystal Structures, 2nd Edition. Vol. 1 by R. W. G. Wyckoff. *Acta Crystallographica* **1965**, *18*, 139–139.